A New Model for Estimating Troposcatter Loss and Delays Based on Ray-Tracing and Beam Splitting With ERA5

Shuang Zhang, Xi-Hong Chen, Qiang Liu, and Xin-Ping Mi

***Abstract*— The atmospheric environment is one of the critical factors affecting troposcatter transmission loss and propagation delay. This article proposes a new estimation model that can accurately calculate troposcatter transmission loss and propagation delay with a numerical weather model (NWM). The ERA5 reanalysis data as the NWM are applied to construct the new model. The 3-D ray-tracing and beam splitting are used to calculate propagation paths and delays. Compared with the existing methods, the new model thoroughly considered the bending and delaying effects of the atmospheric environment on electromagnetic waves, resulting in more accurate estimates. The transmission loss calculation capability of the new model is compared with the International Telecommunication Union (ITU) model and the terrestrial trans-horizon propagation loss data banks. The propagation delay calculation capability is compared with the Bello model. These comparison results show that the new model sufficiently reflects the meteorological environment's influence on transmission loss and propagation delay. Finally, the daily variation characteristics of losses and delays are analyzed using the new model and further validate the model performance.**

***Index Terms*— Estimation model, numerical weather model (NWM), propagation time, time delay extension, trans-horizon propagation, transmission loss, troposcatter.**

I. Introduction

TROPOSPHERIC scattering is an over-the-horizon wireless propagation method that takes advantage of the scattering or reflection of electromagnetic waves by the inhomogeneity of the tropospheric atmosphere. It has the characteristics of narrow beam, low propagation elevation angle, strong barrier crossing ability, high reliability, good resistance to nuclear explosion and interception, and so on. It can be applied to wireless communication [1]–[3], time synchronization [4], [5], and over-the-horizon detection and positioning [6], [7].

The troposcatter channel has the following three characteristics [8]: the first is high transmission losses, most of the energy at the transmitter penetrates the troposphere, and only a small part of energy reaches the receiver by the forward scattering; second, highly sensitive to meteorological influences, affected by the tropospheric dielectric properties, temperature, humidity, and air pressure, the propagation path is curved and the propagation time is delayed. Moreover, the received signal has fast and slow fading characteristics; and the third is the multipath effect. The scattered electromagnetic wave reaches the receiver antenna by multiple transmission paths, and the received signal has a microsecond time delay extension.

The above characteristics are crucial to constructing troposcatter links. The transmission loss determines the distance of troposcatter wireless communication systems, and the multipath time delay extension distorts the transmitted signal waveform, resulting in intercode interference (ICI) or intersymbol interference (ISI) [9], [10]. In the time synchronization systems based on troposcatter, propagation delay is the main source of error that affects time synchronization accuracy, especially for the unidirectional time synchronization systems where time synchronization accuracy is almost entirely determined by delay estimation accuracy [4], [5]. In the troposcatter-based over-the-horizon detection and positioning systems, accurate transmission loss and time delay extension estimation are the basis for accurate positioning. Accordingly, to improve the performance of troposcatter systems, the transmission loss and time-delay variation characteristics of troposcatter links must be accurately estimated.

Many scholars have done extensive research in the estimate and forecast of transmission loss. The database of troposcatter links was developed in the mid-to-late-20th century through many troposcatter link experiments [11], [12]. Three scattering propagation mechanisms were proposed [8]: turbulent incoherent scattering, irregular-layer incoherent reflection, and steady-layer coherent reflection. By combining tropospheric scattering link data with scattering mechanisms, various semiempirical models of tropospheric scattering losses have been developed, such as the NBS method of the U.S. National Bureau of Standards [13], the "French method" proposed by French scientists Battesti *et al.* [14], and the "Chinese" method proposed by Zhang [8] as an alternative to the NBS method (adopted as International Telecommunication Union (ITU)-R P.617-1 method [15], the latest version is ITU-R P.617-5 [16]). In addition to the semiempirical calculation models, multiple loss prediction models based on the scattering propagation mechanism have been generated, such as Zhang's method for calculating the convective layer scattering transmission loss based on the generalized scattering cross section [8],

Manuscript received 26 October 2021; revised 5 January 2022; accepted 6 February 2022. Date of publication 28 March 2022; date of current version 26 July 2022. This work was supported by the National Natural Science Foundation of China (NSFC) under Grant 61701525 and Grant 61671468. *(Corresponding author: Qiang Liu.)*

The authors are with the Air and Missile Defense College, Air Force Engineering University, Xi'an 710051, China (e-mail: dreamlq@163.com).

Digital Object Identifier 10.1109/TAP.2022.3161458

the parabolic equation method proposed by Li *et al.* [17], and the ray-based troposcatter channel model proposed by Dinc and Akan [18], [19]. Based on the above models, some progress has also been made in recent years to improve the loss estimation performance using optimization algorithms, such as in 2016, Li *et al.* [20] used genetic algorithm combined with troposcatter link database to optimize the relevant to-be-determined scaling parameters and combined it with waveguide and layer reflection anomaly propagation model to obtain a new improved model, in 2018, Wei *et al.* [21] derived a distribution model of fast and slow fading characteristics of troposcatter transmission loss based on the fast and slow fading characteristics of electric field strength and combined with the ITU-R P.617-3 model and proposed a transmission loss prediction method based on the transmission loss distribution model, and in 2021, Yuan and Chen [22] used the particle swarm algorithm combined with the troposcatter database to obtain the optimal proportional weights of the three propagation mechanisms in different climate regions for the situation that the three propagation mechanisms of troposcatter may exist simultaneously with different weights in different regions, and the loss prediction capability is better than the ITU recommended algorithm.

In terms of troposcatter propagation time and time delay extension, most existing loss models are not directly solvable and additional link geometry configuration analysis is required. Sunde [23] derived a rough formula for the average time delay difference from the geometric configuration of the link based on a symmetric link and a smooth sphere. Starting with the geometry of the scattering link, Bello [24] deduced a mathematical expression for the delayed power spectrum function based on the Boor–Gordon scattering cross-sectional theory and the 2-D plane assumption. Zhang [8] derived the normalized delay power spectrum based on the generalized scattering cross-sectional theory in combination with the geometric configuration of the troposcatter link. In Ergin Dinc's model, the troposcatter beam was divided into subbeams to calculate the received power and transmission path separately, which provided a convenience to get the transmission loss and time delay extension simultaneously [19].

The above models play an important role in assisting the design of troposcatter communication links, but with the continuous expansion of troposcatter applications, time synchronization systems and over-the horizon detection systems based on troposcatter links have put forward a higher requirement for predicting and analyzing transmission loss and propagation delay under different meteorological environments. The existing models all assumed that electromagnetic waves propagate in a straight line at the speed of light in the atmosphere. The meteorological variate in existing models is generally expressed with empirical fitting values, average statistical results, or standard atmospheric reference models, which cannot give sufficient details about the meteorological environment in different regions and moments, let alone effectively reflect the path bending and propagation speed changes that occurred when radio waves propagate in the complex and variable atmospheric environment. It is necessary to find a more accurate and detailed source of the meteorological environment and construct a new and more precise troposcatter model.

Numerical weather models (NWMs) are a 3-D meteorological information field generated by processing meteorological observations from different sources through physical models based on data assimilation principles, which has the advantages of reliable accuracy, wide usable range, and not limited by space and time. At present, the international mainstream numerical meteorological models have reached the level of 1 h temporal resolution and 0.25° spatial resolution, which can provide sufficiently accurate and reliable meteorological data for troposcatter models.

In this study, the ERA5 Global Atmospheric Reanalysis dataset [25] produced by the European Centre for Medium-Range Weather Forecasts (ECMWF) is applied as the NWM to construct the troposcatter model. The 3-D ray-tracing and beam splitting, as the other two main contributions, are used to calculate propagation paths and delays. Section II briefly introduces the troposcatter principle and the ITU model for calculating transmission loss. The method of extracting meteorological data from ERA5 is described in Section III. In Section IV, an approach for calculating the troposcatter propagation path with 3-D ray-tracing is given, and an algorithm for splitting and aligning the troposcatter beam is proposed. Section V gives the formulas for calculating transmission loss and propagation delay. Finally, in Section VI, the new model results are compared with the ITU model results, the measured data from the data banks, and the Bello model. The daily variation characteristics of transmission loss and propagation delay calculated by the new model are analyzed.

II. Principles of Troposcatter

Among the three existing troposcatter propagation mechanisms, the turbulent incoherent scattering theory is supported by a rigorous turbulence theory, which has a complete theoretical system and is considered the leading cause of troposcatter propagation. The turbulent incoherent scattering theory considers that turbulence is prevalent in the troposphere and filled with vortices, in the common overlap area of the transmitter and receiver beams, the vortex is excited by the transmitting wave and forms a dipole, which reradiates the electromagnetic energy, and a small amount of the reradiated energy enters the receiver antenna, then the electromagnetic waves propagate to the beyond-line-of-sight receiver. The electrical properties of the dipoles in the common overlap region are independent of each other, so the receiver field strength is the sum of the powers of all scatterers in the overlap region. The geometric configuration of the link for tropospheric scattering propagation is shown in Fig. 1, and the meanings of the parameters in Fig. 1 are given in Table I.

The geometric configuration given in Fig. 1 is the basis for constructing a semiempirical prediction model, for the most widely used ITU-R P.617-5 model estimates the average annual median transmission loss distribution for time percentages greater than $p\%$ from

$$L(p) = F + 22\log f + 35\log\Theta + 17\log d + L_c + Y_p \quad (1)$$

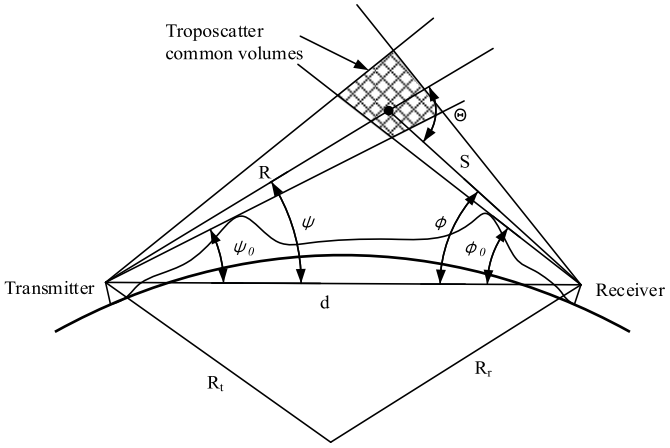

Fig. 1. Geometric configuration of troposcatter link.

TABLE I
PARAMETERS IN TROPOSCATTER LINK

Symbol	Quantity
R_t , R_r	Earth radius at transmitter and receiver
R , S	Distance from the transmitter and receiver to the scatterer
ψ_0 , ϕ_0	Horizon angles of the transmitter and receiver
d	The straight line distance between the receiver and the transmitter
ψ , ϕ	The angle between R , S and d
Θ	Scattering angle

where

$$F = 0.18 \cdot N_0 \cdot \exp(-h_s/h_b) - 0.23 \cdot dN \tag{2}$$

where f is the electromagnetic wave frequency, L_c is the aperture-medium coupling loss, Y_p is the function related to the probability p, h_s is the height of the earth's surface above sea level, and h_b is the scale height, which can be determined statistically for different climates conditions. For reference purpose, a global mean of the scale height may be defined by $h_b = 7.35$ km. N_0 is the average annual sea-level refractive index of the link, dN is the radio-refractive index lapse rate through the lowest 1 km of the atmosphere, and only N_0 and dN are related to the meteorological environment. ITU has provided annual average values of N_0 and dN in different regions of the world. Obviously, this method cannot effectively reflect the influence of complex and variable meteorological environments on the transmission loss, and more detailed and accurate meteorological data must be used in the new model.

III. EXTRACT METEOROLOGICAL DATA FROM ERA5

The ERA5 is the latest version of the reanalysis produced by ECMWF, which is available at $0.25° \times 0.25°$ spatial resolution and 1 h temporal resolution, and provides the atmospheric parameters at 37 vertical pressure levels from 1000 to 1 hPa. The meteorological data of ERA5 are stored on the nodes of the grid structure [26]. In order to obtain meteorological data for a given location, the ERA5 elevation system has to be converted before interpolating the meteorological data.

A. Elevation System Conversion

The ERA5 reanalysis dataset provides geopotential height, whereas the path calculation is carried out in the global geodetic coordinate system. Convert the geopotential height to geodetic height from

$$H_g = H_\phi g_0 / \overline{g_s}(\varphi, \lambda, H_g) \tag{3}$$

where $g_0 = 9.80665\ \text{ms}^{-2}$ is the standard value of the acceleration of gravity and $\overline{g_s}(\varphi, \lambda, H_g)$ represents the average acceleration of gravity along the plumb line to the geoid

$$\overline{g_s}(\varphi, \lambda, H_g) = \frac{1}{H_g} \int_0^{H_g} g(\varphi, \lambda, H_g) \mathrm{d}h \tag{4}$$

and $\overline{g_s}(\varphi, \lambda, H_g)$ can be further expressed through the universal gravity formula as

$$\overline{g_s} = \frac{1}{H_g} \int_0^{H_g} \frac{GM_e}{(h + R_e)^2} \mathrm{d}h = \frac{GM_e}{R_e(H_g + R_e)}. \tag{5}$$

Equation (5) contains the unknown variable H_g, which an iterative algorithm can solve. At initial as $H_g(0) = H_\phi g_0/9.81$, and bring into the following formula [27] for iterative calculation:

$$\begin{cases} H_g(n+1) = \dfrac{H_\phi g_0 R_e [H_g(n) + R_e]}{GM_e} \\ R_e = \dfrac{6378137}{1.006803 - 0.006706 \sin^2 \varphi} \end{cases} \tag{6}$$

where φ is the latitude of the point. The above iterative algorithm has been verified that the accuracy could converge to a millimeter scale after several iterative steps.

B. Meteorological Data Interpolation 0

The meteorological parameters used in this study include temperature, specific humidity, atmospheric pressure, the eastward component of the horizontal wind, and the northward component of the horizontal wind. The ERA5 dataset provides meteorological data at grid points with a horizontal interval of 0.25° and 37 levels in the vertical direction. The data at nongrid points have to be obtained by interpolation or extrapolation.

When the interpolation points are located inside the grid, bilinear interpolation is used for all meteorological parameters in the horizontal direction. In the vertical direction, linear interpolation is used for temperature, specific humidity, and wind speed, and exponential model interpolation [28] is used for pressure as

$$\begin{cases} P = 0.01 P_0 \exp\left(-\dfrac{g_0 \mathrm{d}h \mathrm{dMtr}}{R_g T_v}\right) \\ T_v = T_0(1 + 0.6077\ q_0) \end{cases} \tag{7}$$

where P_0, T_0, and q_0 are the air pressure, temperature, and specific humidity at grid points, respectively, dh represents the elevation difference between the interpolation and grid point, $\mathrm{d}Mtr = 28.965 \cdot 10^{-3}$ kg/mol is the molar mass of dry air, and $R_g = 8.3143$ J/K·mol is the gas constant.

When the interpolation point is below the lowest level of the grid, bilinear interpolation is still applicable in the horizontal direction, but in the vertical direction, some other empirical methods are required. Temperature values are calculated using a common approach to global meteorological modeling, assuming a constant temperature gradient of −0.0065 °C/m [29]. Specific humidity is constant below the lowest grid point, as recommended by the ERA5 user manual [30]. Pressure is still calculated using the exponential model. Wind speed is calculated with the power-law extrapolation model as [31]

$$v_c = v_1 \left(\frac{h_c}{h_1} \right)^{\alpha} \tag{8}$$

where h_c represents the height of the extrapolation point, h_1 denotes the height of the grid point, v_1 is the wind speed obtained by bilinear interpolation in the horizontal direction, and α is the wind shear index, which is set for different terrain conditions.

When the interpolation points are located above the highest level of the grid, the CIRA86 International Reference Atmosphere Model is used to obtain meteorological data.

C. Refractivity of Atmosphere

The atmospheric refractivity is a crucial intermediate parameter for the electromagnetic wave propagation. The refractivity N is calculated from

$$N = k_1 \frac{P_d}{T} + k_2 \frac{e}{T} + k_3 \frac{e}{T^2} \tag{9}$$

where P_d, e, and T are the dry air pressure, water vapor pressure, and temperature, respectively, k_1, k_2, and k_3 are the atmospheric refraction coefficients, which have slightly difference in [33] and [34]; in this study, $k_1 = 77.6890 \times 10^{-2}$ k/hPa, $k_2 = 71.2952 \times 10^{-2}$ k/hPa, and $k_3 = 375.463 \times 10^3$ k^2/hPa the same with [33].

The ERA5 provides total atmospheric pressure p, temperature T, and specific humidity q directly. The water vapor pressure e needs to be calculated by specific humidity. Thus, in the actual refractivity calculation, the formula is used as follows:

$$\begin{cases} N = k_1 \dfrac{P}{T} + \left(k_2' \dfrac{e}{T} + k_3 \dfrac{e}{T^2} \right) \\ k_2' = k_2 - k_1 \dfrac{R_d}{R_v} \\ e \approx \dfrac{q P}{(0.62198 + 0.37802 q)} \end{cases} \tag{10}$$

where $R_d = 287.0597$ J/kg·K and $R_v = 461.525$ J/kg·K are dry air gas constant and water vapor gas constant, respectively.

IV. Troposcatter Path Based on 3-D Ray-Tracing

A. Central Ray Path of the Troposcatter Beam

Electromagnetic wave propagation paths can be solved by geometric optical ray theory when the refractivity varies very little over a wavelength range [36]. Troposcatter usually uses the microwave band, the refractivity varies negligibly over one wavelength range in the microwave band, so the propagation path can be solved using the geometric optics theory. The 3-D ray-tracing method is applied to calculate the path of electromagnetic wave propagation based on Fermat's law of geometrical optics theory as

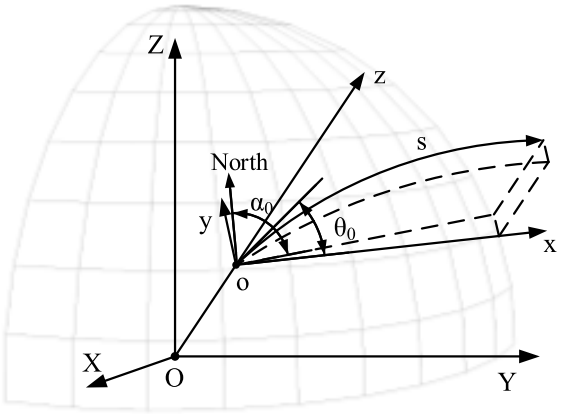

Fig. 2. Coordinate system for 3-D ray tracing. (X, Y, Z) is the local spherical geocentric right-angle coordinate system with the origin at the center of the earth, (x, y, z) is the local right-angle coordinate system with the origin at the transmitter, and θ_0 is the angle between the initial direction of the ray and the horizon, i.e., the initial elevation angle.

$$\delta t = \delta \frac{1}{c} \int_S n ds = 0 \tag{11}$$

where c is the light speed in vacuum, t is the propagation time, s is the propagation path, and $n = N \cdot 10^{-6} + 1$ is the atmospheric refraction index, and N can be calculated using (10) based on the ERA5 meteorological data.

In order to improve model computational efficiency, the local sphere rather than the earth ellipsoid is applied in the 3-D ray-tracing. The origin of the local sphere is the center of the earth, and the sphere's radius is calculated using Euler's formula [38] based on the mean latitude of the receiver and transmitter. The formula is as follows:

$$\begin{cases} R = \dfrac{MN}{M \sin^2 \alpha + N \cos^2 \alpha} \\ M = \dfrac{a(1 - e^2)}{(1 - e^2 \sin^2 \varphi')^{1.5}}, \quad N = \dfrac{a}{\sqrt{1 - e^2 \sin^2 \varphi'}} \end{cases} \tag{12}$$

where α denotes the earth azimuth of the receiver and transmitter, φ' is the mean latitude of the receiver and transmitter, a is the long semiaxis of the earth ellipsoid, and e is the first eccentricity of the earth ellipsoid. In this study, the WGS-84 coordinate system is applied, and the long semiaxis $a = 6378137$ m and the short semiaxis $b = 6356752.3142$ m.

The vertical direction of the troposcatter propagation path is more curved than the horizontal direction. A local coordinate system is constructed based on the local spherical coordinate system to simplify the solution process further. The local right-angle coordinate system is established based on the right-handed spiral criterion, with the x-axis being the projection of the initial direction of the ray onto the tangent plane of the earth's surface and the z-axis being the directional vector from the earth sphere center to the location of the transmitter, as shown in Fig. 2.

In (x, y, z), the ds of (11) can be expressed as follows:

$$\begin{cases} ds = \sqrt{dx^2 + dy^2 + dz^2} = \sqrt{1 + y'^2 + z'^2}dx \\ y' = dy/dx, z' = dz/dx. \end{cases} \tag{13}$$

Let function H

$$H(x, y, z, y', z') = n(x, y, z)\sqrt{1 + y'^2 + z'^2}. \tag{14}$$

Equation (11) can be expressed as

$$\delta \int_s H(x, y, z, y', z')dx = 0. \tag{15}$$

Derive from the variational method. The Euler equation is obtained as

$$\begin{cases} \dfrac{\partial H}{\partial y} - \dfrac{\mathrm{d}}{\mathrm{d}x}\dfrac{\partial H}{\partial y'} = 0 \\ \dfrac{\partial H}{\partial z} - \dfrac{\mathrm{d}}{\mathrm{d}x}\dfrac{\partial H}{\partial z'} = 0. \end{cases} \tag{16}$$

In addition, the index of refraction in the local right-angle coordinate system has

$$\frac{dn}{dx} = \frac{\partial n}{\partial x} + \frac{\partial n}{\partial y}y' + \frac{\partial n}{\partial z}z'. \tag{17}$$

Bringing (17) into (16) and expanding, we can obtain the system of linear differential equations [38]

$$\begin{cases} y'' = \dfrac{1 + y'^2 + z'^2}{n}\left(-y'\dfrac{\partial n}{\partial x} + \dfrac{\partial n}{\partial y}\right) \\ y'' = \dfrac{1 + y'^2 + z'^2}{n}\left(-z'\dfrac{\partial n}{\partial x} + \dfrac{\partial n}{\partial z}\right). \end{cases} \tag{18}$$

The solution of (18) depends on the definition of initial conditions. In (x, y, z), the ray starting point is the coordinate origin o, and the initial incidence angle of the ray θ_0 is in the xoy plane. Thus, the initial boundary condition of (18) can be expressed as

$$\begin{cases} y|_{x=0} = z|_{x=0} = 0 \\ z'|_{x=0} = \tan\theta_0 \\ y'|_{x=0} = 0. \end{cases} \tag{19}$$

The propagation path from the transmitter to the top of the troposphere is obtained by numerically solving the linear differential (18) subject to the initial boundary conditions (19). In this study, the fourth- and fifth-order Runge–Kutta algorithm are used to solve the differential equation system, and balancing computational efficiency and accuracy by setting appropriate relative and absolute errors, we set relative and absolute error 10e-5.

From Fig. 1, the troposcatter path is the entire path from the transmitter to the scattering point to the receiver. Thus, the scattering point and the path from the scattering point to the receiver also need to be calculated. With known receiver position and antenna elevation angle, the receiver is treated as a transmitter, and the propagation path is calculated in the same way as above. Theoretically, the intersection of the receiver and transmitter path is the scattering point, but given the horizontal inhomogeneity of the tropospheric atmosphere, the two paths usually do not intersect precisely at one point; therefore, an alignment algorithm needs to be applied to adjust the ray path, and we will describe it in Section IV-B.

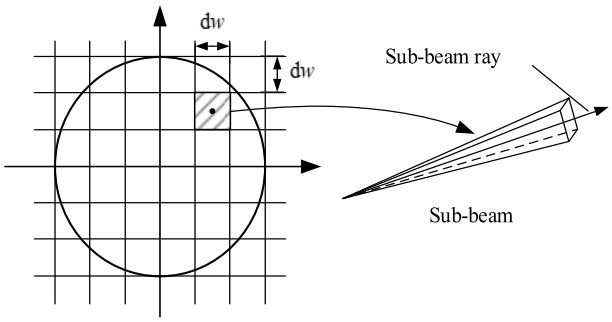

Fig. 3. Diagram of transmitter beam decomposition. Each square with a center point within the beam boundary corresponds to a subbeam and ray.

B. Beam Splitting and Alignment

Tropospheric scattering is a typical multipath transmission channel, and a single center ray of antenna spindle cannot reflect the actual situation of the channel. In this study, we split the troposcatter beam into several densely arranged subbeams that do not interfere with each other. Analyze and calculate each subbeam separately.

Irrespective of the path bending due to the atmospheric refraction, we assumed that the antenna emits a cone-shaped beam (the vertical and horizontal widths of the beam are equal), and the 3 dB beamwidth of the antenna is the boundary of the conical beam. The transmitter beam is dissected into a series of closely spaced quadrilateral cones at equal angular dw intervals along the transverse and longitudinal axes of the beam cross section, as shown in Fig. 3.

Let the transmitter beam be split into W equal parts in the transverse and longitudinal directions, the subbeam ray elevation and azimuth angles in (x, y, z) can be expressed as

$$\begin{cases} \theta_{0\_ij} = \theta_0 + dw \cdot i \\ \alpha_{0\_ij} = \alpha_0 + dw \cdot j \\ i, j = -W/2, -W/2 + 1, \ldots, W/2 - 1, W/2 \end{cases} \tag{20}$$

where i and j are the serial numbers of the transverse and longitudinal profiles of the beam, respectively.

Each subbeam path is bent by the atmosphere's refractive index and needs to be solved on each ray, which would significantly diminish the efficiency of the model. Considering the narrow width of the troposcatter beam, the refractive index change along the propagation direction is basically the same for each subbeam, and the bending degree of each subbeam can be assumed to be the same. Thus, in this study, we obtain the subbeam ray path by rotating the central ray path.

For the transmitter beam, the central ray path is calculated by (18), and the difference in elevation $dw \cdot i$ and azimuth $dw \cdot j$ between the subbeam ray and the central ray is obtained from (20), and then rotating the central ray path by the appropriate angle in 3-D space gives the subbeam ray path.

The beam splitting method of the receiver is different from the transmitter. According to the turbulent incoherent scattering theory, the dipoles within the common scatterer can be propagated to the receiver antenna by the forward scattering. One transmit subbeam will correspond to multiple receive subbeams, which in the ray model means that one

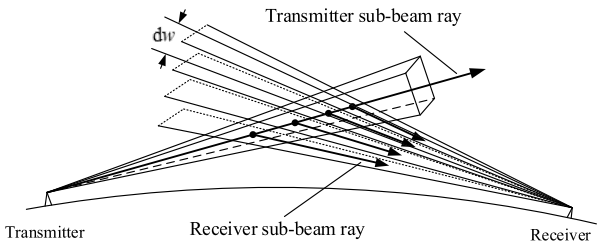

Fig. 4. Diagram of receiver antenna beam splitting. The 3 dB beamwidth of the receiving antenna is transversely segmented with equal angular interval. One transmitter ray has multiple receiver rays.

transmit ray corresponds to multiple receive rays. In order to simulate the above scattering process at the receiver, the received beam is split in the manner shown in Fig. 4.

First, (18) is used to calculate the propagation path of the receiver antenna central ray path and then rotate the central ray path at equal interval angle dw in the pitching direction within the 3 dB width beam to obtain M subbeam ray paths with the same azimuth and different elevation angles. For each transmitter subbeam ray, the minimum distance point and the minimum distance between the M receiver subbeam paths and the transmitter subbeam path are calculated separately, as the ray paths are usually not intersected in 3-D space, and an alignment algorithm is proposed here.

1) Obtain the nearest point of the transmitter and receiver ray paths.
2) Calculate the included angle of the two nearest points about the receiver.
3) Rotating the receiver ray path azimuth according to the included angle.
4) Iterating until the minimum distance is less than the set threshold (the threshold set in this study is 1 m, and it has been verified that mostly the minimum distance can be reduced to 1 m in less than five iterations).
5) Verify and remove the receiver ray paths with azimuth outside the 3 dB receiving antenna beam boundary.

The complete troposcatter subbeam ray paths can be obtained by the method in this section.

V. Troposcatter Transmission Loss and Propagation Delay

A. Basic Transmission Loss

The received power of the subbeam can be calculated with the two-base radar equation [24]

$$P_{r\_l} = \frac{P_{t\_l} G_t G_r g_t g_r \sigma_l \lambda^2}{(4\pi)^3 R_l^2 S_l^2} dV_l \tag{21}$$

where P_{r_l} represents the received power for subbeam l, P_{t_l} is the subbeam transmitting power, G_t and G_r, respectively, donate the transmitting and receiving antenna gain, g_t and g_r are the directivity function of transmitting and receiving antenna, respectively, λ is the wavelength, dV_l is the volume of the common scatterer of this subbeam, R_l and S_l, respectively, are the distances from scattering points to transceiver antennas, and σ_l is the scattering cross section to the subbeam.

G_t and G_r can be obtained by the empirical formula

$$G_{t,r} = 10\lg\left(4.5(D/\lambda)^2\right) \tag{22}$$

where D is the antenna diameter. The beamwidth ω can be determined by antenna diameter and wavelength

$$\omega = 1.2\frac{\lambda}{D}. \tag{23}$$

Assume that the vertical width of the beam is the same as the horizontal width, let the antenna directivity function is Gaussian, the g_t and g_r can be expressed as

$$\begin{cases} g_t = \exp\left(-\dfrac{4\ln 2}{\psi_1^2}\left[(\theta_1-\theta_{10})^2+(\alpha_1-\alpha_{10})^2\right]\right) \\ g_r = \exp\left(-\dfrac{4\ln 2}{\psi_2^2}\left[(\theta_2-\theta_{20})^2+(\alpha_2-\alpha_{20})^2\right]\right) \end{cases} \tag{24}$$

where ψ_1 and ψ_2 represent the transceiver beamwidths, θ_1 and θ_2 are the transceiver antenna elevation angles, α_1 and α_2 are the transceiver antenna azimuth angles, θ_{10} and θ_{20} are the transceiver antenna spindle elevation angles, and α_{10} and α_{20} are the transceiver antenna spindle azimuth angles.

The subbeam scattering cross section σ_l is based on Kolmogorov's theory and can be expressed as

$$\sigma_l = 2\pi k^4 \cos(\Theta_l)^2 \Phi(k_l) \tag{25}$$

where $k = 2\pi/\lambda$ is the wavenumber, Θ_l is the subbeam ray scattering angle, and $\Phi(k_l)$ is the spatial spectral function obtained by the Kolmogorov–Obukhov law

$$\Phi(k_l) = 0.033 C_n^2 (2k\sin(\Theta_l/2))^{-11/3}. \tag{26}$$

The refractive index structure constants C_n^2 in (26) can be calculated by the Tatarski formula [39] as

$$C_n^2 = 2.8 L_0^{4/3} M^2 \tag{27}$$

where M is the refractive index gradient, which can be calculated by (10), and L_0 is the outer scale of turbulence, and it can be calculated by the HMNSP99 outer scale model [40]

$$\begin{cases} L_0^{4/3}(h) = 0.1^{4/3} \times 10^{0.362+16.728\times S-192.347\frac{dT}{dh}} \\ S = \left[\left(\dfrac{\partial u}{\partial h}\right)^2 + \left(\dfrac{\partial v}{\partial h}\right)^2\right]^{1/2} \end{cases} \tag{28}$$

where dT/dh is the temperature gradient, u and v are the latitudinal and longitudinal wind speed, respectively, and S is the wind shear.

B. Common Scatterer Volume

Equation (21) shows that the received power is proportional to dV_l. Dinc and Akan [19] use the following approximate formula in his ray model to calculate the volume:

$$dV_l = \frac{R_l^2 S_l^2 (dw)^2}{\sqrt{R_l^2 + S_l^2}\sin(\Theta_l)}. \tag{29}$$

Equation (29) was derived from an approximation in [41] for calculating the common volume of scattering from narrow beams

$$V = 1.206\frac{R^2 S^2 \psi_{v1}\psi_{v2}\psi_{h1}\psi_{h2}}{\left[R^2\phi_1^2 + S^2\phi_2^2\right]^{1/2}\sin\Theta} \tag{30}$$

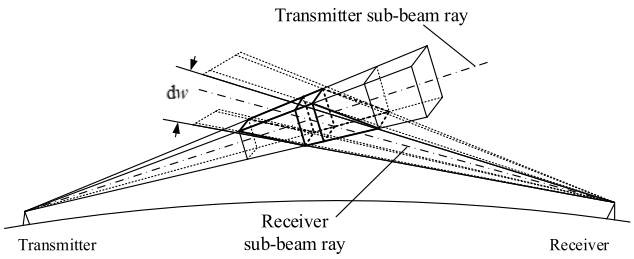

Fig. 5. Common scatterer of subbeam.

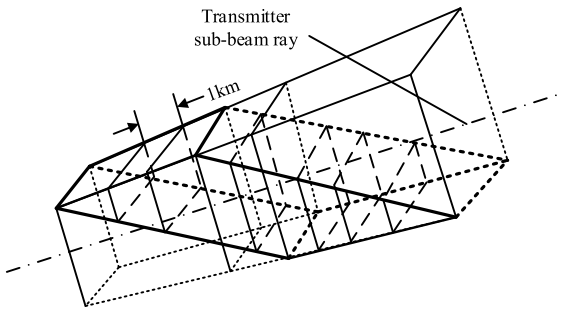

Fig. 6. Dissected the scatterer polyhedron with intervals of 1 km along the direction of the transmitting subbeam.

where Θ is the scattering angle and ψ_{v1}, ψ_{v2} and ψ_{h1}, ψ_{h2} are the vertical and horizontal beamwidths of transceiver antennas. As mentioned in [41], this equation is applicable when Θ is much larger than $\psi_{v1} + \psi_{v2}$. However, in troposcatter, the antenna beam propagates along the horizon to reduce transmission losses. The scattering angle is of the same scale as the beamwidth. Formula (29) does not apply to calculate the volume of the scattering commons in troposcatter.

This article assumes that the antenna beam is a conical beam with the same beamwidth vertically and horizontally. The conical beam is split into smaller quadrilateral conical subbeams. The common scattering area of subbeams can be considered a part of the transmitter subbeam contained in the quadrilateral cone cut by two planes intersecting at the receiver at an angle dw. The black bolded wireframe polyhedron shown in Fig. 5 is the common scatterer of the subbeam.

In the low elevation troposcatter, the common scatterer has a long length along the propagation direction (common scatterer length up to 15 km at a transmitter–receiver distance of 150 km and a beam elevation angle of 0°). If the refractive index gradient at the center of the scatterer is applied as the refractive index of the whole scatterer in (27), significant deviations are introduced. In this article, the scatterer polyhedron is dissected into small trapezoidal bodies (dissecting interval of 1 km) along the direction of the transmitter subbeam ray, as shown in Fig. 6, and the volume of each trapezoidal body is calculated separately using the trapezoidal body volume formula. Then, the refractive index gradient is applied at the center of each trapezoidal body separately.

From (25) and (26), the received power of the subbeam is also related to the scattering angle Θ_l. The subbeam ray path is bent with a large angle in the vertical direction and a slight angle in the horizontal direction (the horizontal bend angle is only about 0.01 mrad for the propagation distance of 100 km at an elevation angle of 0°). As shown in Fig. 7, the ray bending results in a lower actual scattering point, a smaller scattering angle $\Theta_{l\_}$, a more extensive scattering cross section, and spatial spectral function. The effects are equivalent to raise the ground height of the transmitting and receiving antennas. Therefore, the scattering angle $\Theta_{l\_}$ calculated from the tangential angle between transmitter ray path and receiver ray path at the scattering point rather than Θ_l is applied in (25) and (26).

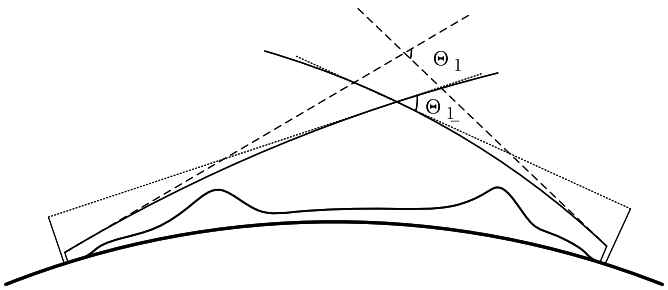

Fig. 7. Bending of the ray makes the scattering angle smaller, which is equivalent to increasing the antenna height.

The received power of each trapezoidal body is obtained by bringing the meteorological data at the position of the trapezoidal body, the scattering angle $\Theta_{l\_}$, and the trapezoidal body volume into (21)–(28). Then, the received power of the subbeam is the sum of the received power of each trapezoidal body.

C. Attenuation by Atmospheric Gases

In addition to the basic transmission loss, the attenuation of electromagnetic power caused by dry air and water vapor in the atmosphere can contribute to a reduction in received power. The attenuation is related to the frequency of propagation, the air pressure, temperature, and water vapor pressure, and the higher the frequency, the farther the propagation distance, the greater the absorption loss. Troposcatter propagates over long distances at low propagation elevation angles, and the attenuation by the atmospheric gases cannot be ignored. Since the ERA5 can provide meteorological data along the propagation path, we calculate the subbeam path gaseous attenuation using the line-by-line summation method recommended by the ITU-R P.676-12.

The atmospheric absorption loss L_l^{γ} of subbeam can be expressed as the integral of the atmospheric specific attenuation γ on the propagation path

$$L_l^{\gamma} = \sum_{j=1}^{j\_\max} a_{l\_j}\gamma_{l\_j} \tag{31}$$

where $j\_\max$ is the total number of line segments consisting of two adjacent data points in the subbeam ray propagation path, a_{l_j} is the length of the line segment between the j path point and the $j+1$ path point in the subbeam ray propagation path array, and γ_{l_j} is the atmospheric specific attenuation, which can be calculated using the ITU-R P.676-12 method [42] based on ERA5 meteorological data.

D. Troposcatter Transmission Loss

By considering the effect of atmospheric absorption attenuation on the received power, the troposcatter subbeam transmission loss can be expressed as

$$L_l = 10\lg\frac{P_{t\_l}}{P_{r\_l}} + L_l^{\gamma} \tag{32}$$

where L_l^{γ} is the subbeam atmospheric absorption loss, P_{t_l} is the subbeam transmit power, and P_{r_l} is the received power, which is the sum of the subdivided trapezoidal bodies received power

$$P_{r\_l} = \sum_{m=1}^{m\_\max} P_{r\_l\_m} \tag{33}$$

where $m\_\max$ is the total number of trapezoidal body in the subbeam.

The subbeam received power is corrected for the effect of atmospheric absorption attenuation to

$$P'_{r\_l} = P_{t\_l} \cdot 10^{-0.1L_l}. \tag{34}$$

Then, the troposcatter transmission loss can be calculated by

$$L = 10\lg\frac{P_t}{\sum_{l=1}^{l\_\max} P'_{r\_l}}. \tag{35}$$

E. Troposcatter Propagation Delay

The troposcatter propagation time can be expressed in two parts: the first part is the ranging delay time due to the slowing down of the electromagnetic wave propagation speed; the second part is the propagation time of the electromagnetic wave along the curved path from the transmitter point through the scattering point and then to the receiver point at the speed of light. Generally, the propagation time is expressed in the form of propagation distance as

$$L_{total} = \int_{S_t+S_r} n ds = \underbrace{\int_{S_t+S_r} (n-1) ds}_{L_v} + \underbrace{\int_{S_t+S_r} ds}_{L_c} \tag{36}$$

where S_t and S_r are, respectively, the propagation paths of the transmitter and receiver, L_v is the ranging delay, and L_c is the bending path length.

Different subbeams have different propagation times. The low elevation angle subbeam propagation time is shorter, the high elevation angle subbeam propagation time is longer, and let the longest propagation distance of all subbeams is $L_{total\_\max}$, and the shortest propagation distance $L_{total\_\min}$, then the troposcatter time delay extension $\Delta\tau$

$$\Delta\tau = \frac{L_{total\_\max} - L_{total\_\min}}{c}. \tag{37}$$

The normalized delay power spectrum of the troposcatter link can be obtained by normalizing the received power of all subbeams and arranging the propagation time in ascending order.

VI. Model Validation and Analysis

To facilitate later description, the model proposed in this article is abbreviated as RTBS_ERA5.

A. RTBS_ERA5 Transmission Loss Validation

Ten troposcatter links are selected from the "measured and predicted long-term distributions of tropospheric transmission loss" by the Office of Telecommunications Report OT/TRER 16 [12]. The RTBS_ERA5 model is compared with ITU-R P.617-2 and ITU-R P.617-5. The parameters of the ten links are shown in the Appendix.

From (1), the scattering angle Θ is the key to the loss calculation in the ITU model, which is calculated as [15], [16]

$$\Theta = D \cdot 10^3/ka + \psi_0 + \phi_0 \tag{38}$$

where k is the effective earth radius factor at the median refractive index, a is the earth radius, and ψ_0 and ϕ_0 are, respectively, the horizon angle of the transmitting and receiving antennas, determined by the altitude of the obstacles distributed in the scattering path and the distance to the antenna.

The ITU model uses the horizon angle rather than the actual antenna elevation angle and does not consider the effect of beamwidth. In contrast, the RTBS_ERA5 uses the actual antenna elevation angle and beamwidth to calculate the results accurately. Considering that Report OT/TRER 16 has no data about the antenna elevation and beamwidth, it is necessary to obtain the antenna elevation and beamwidth before comparing.

In the construction of the link, troposcatter generally uses the low elevation angle to reduce losses, and the antenna is adjusted to the best elevation angle with the lowest loss in the local meteorological environment. However, the best elevation angle varies with the meteorological environment, and it is not possible to calculate the best elevation angle at different times one by one in the validation. In this study, the RTBS_ERA5 model is applied to obtain the antenna elevation angle with the lowest transmission loss using the iterative step algorithm based on the meteorological data on January 1, 2020.

The 3 dB beamwidth of the antenna is obtained through the antenna gain. The antenna gain for the ten links is provided by the China Research Institute of Radiowave Propagation (CRIRP).

Table II gives the measured median values of the transmission losses of the ten links relative to free space and the calculation results of the three models. The meteorological data used for the RTBS_ERA5 are the monthly averages of ERA5 over the time range of the link observations.

The results of the RTBS_ERA5 model are better than the two ITU models in terms of mean and rms error, and ITU-R P.617-5 is better than ITU-R P.617-2. The results of the two ITU models are smaller than the measured median, and the RTBS_ERA5 model is slightly larger than the measured median.

The transmission loss is closely related to the elevation angle. Fig. 8 presents the three models' results for the two links LT2063 and LT2307 at different elevation angles. Considering that the ITU model uses the horizon angle rather than the

TABLE II
ERROR COMPARISON OF THREE METHODS

Path	Measured value（dB）	Measurement year	Calculation error relative to measured value（dB）		
			ITU-R P.617-2	ITU-R P.617-5	RTBS_ERA5
LT0908	78.1	1953-1955	1.7	4.1	6.9
LT1440	66.9	1953-1954	-13.6	-5.2	2.8
LT1441	84.0	1953-1954	-9.1	-7.9	-4.7
LT2063	70.4	1958-1959	4.4	-4.4	-3.5
LT2272	70.8	1960-1962	-8.0	-2.9	1.4
LT2273	73.5	1960-1962	3.6	4.3	6.1
LT2304	69.0	1958-1959	-4.6	0.2	4.4
LT2305	61.2	1958-1959	-5.6	-1.5	2.1
LT2306	90.3	1958-1959	-14.7	-14.4	-9.7
LT2307	68.3	1959	-3.0	-3.1	-0.37
Mean of error			-4.89	-3.08	0.55
RMS of error			6.37	5.26	4.93

actual elevation angle, the horizon angle is assumed to increase in parallel with the elevation angle in the comparative analysis.

Fig. 8 shows that the transmission loss increases with the elevation angle, and the difference between the models is slight at low elevation angles. As the elevation angle increases, the difference tends to become more significant. The ITU-R P.617-2 model gives much higher values at high elevation angles than the RTBS_ERA5 and ITU-R P.617-5. The difference between the RTBS_ERA5 model and ITU-R P.617-5 also increases with elevation angle, but the magnitude of the difference is smaller than the difference between ITU-R P.617-2 and RTBS_ERA5.

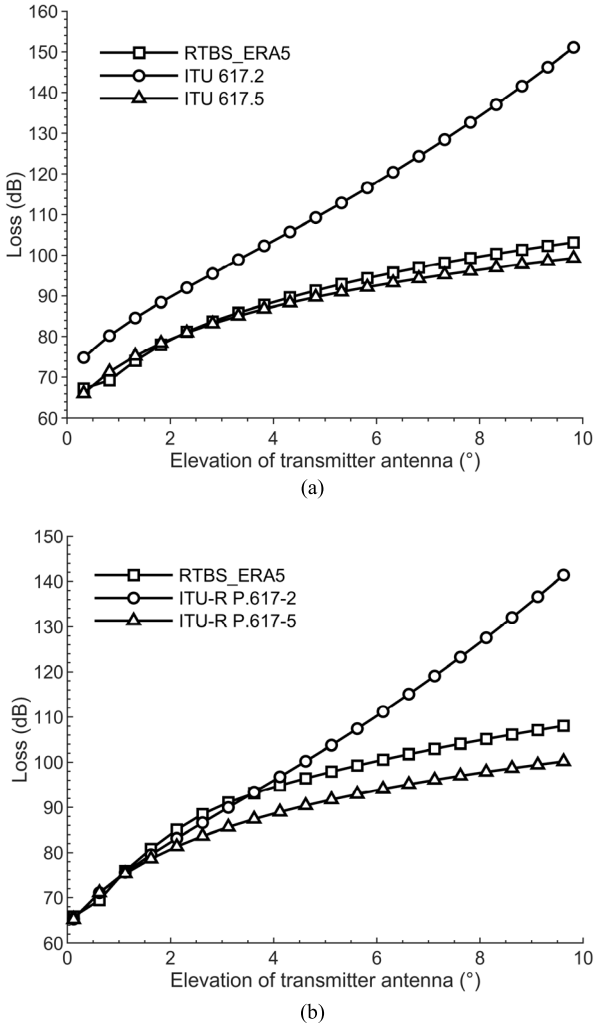

Fig. 8. Transmission loss changes of (a) LT2063 and (b) LT2307 at different elevation angles.

B. Analysis of Daily Transmission Loss of RTBS_ERA5

The links LT1441 and LT2305 in the Appendix are selected to analyze the variation characteristics of troposcatter transmission loss. LT1441 is located in Newfoundland Island, Canada, 277 km long, with the scattered link partially passing through the sea bay; LT2305 is located between Tokyo and Fukushima, Japan, 226 km long, with the scattered link passing through an area of land. The locations of the two links are shown in Fig. 9. The hour-by-hour transmission loss calculated using the RTBS_ERA5 on August 25–27, 2020, is given in Fig. 10.

As seen from Fig. 10, the RTBS_ERA5 has successfully obtained the hour-by-hour transmission loss variation through the ERA5 meteorological data. Both links show a tendency of alternating diurnal loss variation, with daytime loss increasing and nighttime loss decreasing, but the diurnal rise and fall are not consistent. The LT1441 link is adjacent to the Atlantic Ocean and passes through the sea bay, and the meteorological environment is complex and changeable. The transmission loss varies widely at different times. The maximum hourly variation can be 6.3 dB, and the maximum diurnal loss fluctuation of 20.4 dB; the LT2305 link passes through the land area, the meteorological conditions are relatively stable, the loss variation is slight, the maximum hourly variation is 2.4 dB, and the maximum diurnal loss fluctuation of 5.3 dB, with a cyclical pattern of loss variation.

C. RTBS_ERA5 Propagation Delay Validation

Comparing RTBS_ERA5 with Bello's delayed power spectrum calculation method, the Bello model formula is [19]

$$\phi_h(\tau)d\tau \propto \int_{\psi_0}^{\psi_1} \frac{g_t(\psi-\psi_0)g_r(\phi-\phi_0)}{0.25\psi^3\phi^2(\psi+\phi)^{m-2}}d\psi d\tau \qquad (39)$$

where $\propto$ means "proportional to," $\phi_h(\tau)$ denotes the average power with delay τ, i.e., the delayed power spectrum of the channel, ψ_1 and ψ_0, respectively, denote the maximum and minimum values of ψ, ψ_1 corresponds to the case when ϕ takes the minimum value ϕ_0, and m is the scattering parameter and takes the value of 5. The delay power spectrum is obtained by calculating and normalizing the average power over the entire delay range.

In order to analyze the performance of the two models, six links with different distances and beam widths are set up, and the parameters of the links are shown in Table III and the

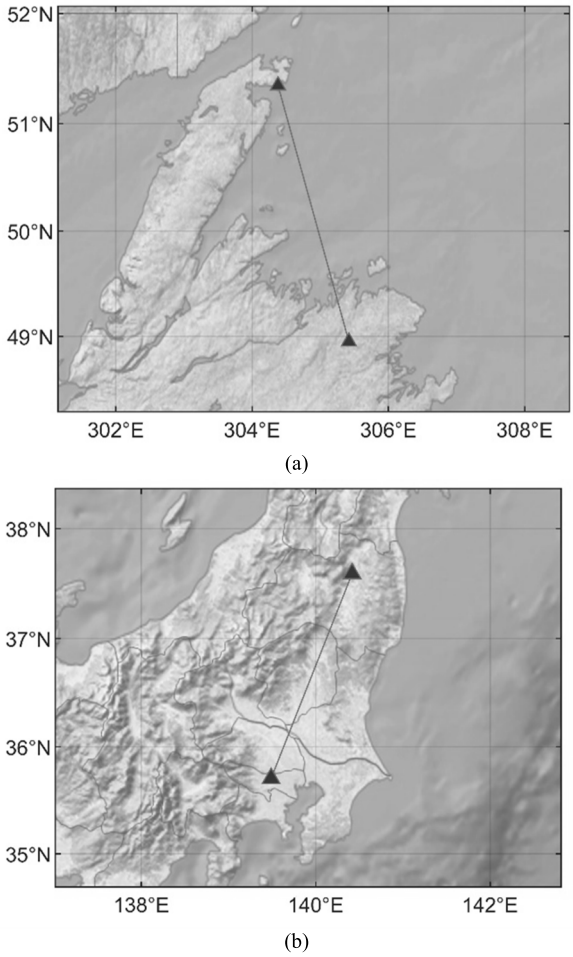

Fig. 9. Geographical locations of (a) LT1441 and (b) LT2305.

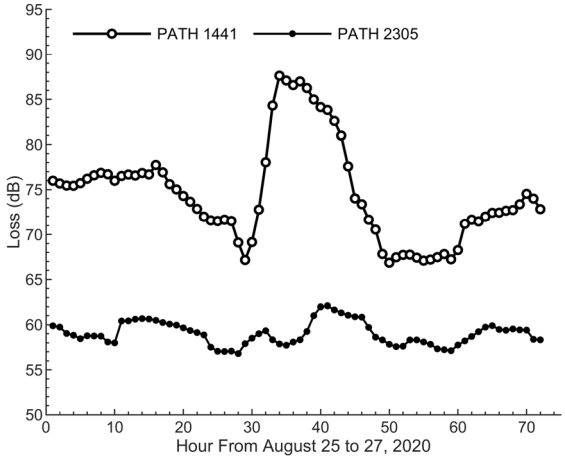

Fig. 10. Hour-by-hour changes in transmission loss for LT1441 and LT2305 from August 25–27, 2020.

normalized delay power spectra calculated for the two models are given in Fig. 11.

From Fig. 11, the RTBS _ERA5 and the Bello model have essentially the same delay power distribution. With the same beamwidth, the further the distance, the greater the propagation time and the wider the delay extension; compare Fig. 11(c) and (d), with the same distance, the wider the beam, the greater the delay extension.

TABLE III
LINK PARAMETERS USED TO COMPARE PROPAGATION DELAY

Path	Transmitter longitude / latitude (°)	Receiver longitude / latitude (°)	Distance (km)	Beamwidth (degree)
1	32.8451/114.0265	34.0936/115.0274	166	2.4
2	32.8451/114.0265	34.7178/115.5278	250	2.4
3	32.8451/114.0265	35.3421/116.0282	333	2.4
4	32.8451/114.0265	35.3421/116.0282	333	1.2
5	32.8451/114.0265	35.9663/116.5286	415	1.2
6	32.8451/114.0265	36.5905/117.0290	498	1.2

Another critical point to highlight in Fig. 11 is the offset in the distribution of delay spectra between the RTBS_ERA5 and Bello models, and the propagation time of RTBS_ERA5 is longer than the Bello model, which is attributed to the fact that the Bello model derives the propagation delay from the geometry of the scattering link. The Bello model assumes that the wave travels at the speed of light in a straight line and does not consider the influence of the atmospheric environment. In contrast, the RTBS_ERA5 precisely calculates the bending and delay of the wave propagation path.

Table IV gives the statistical results on the minimum propagation time, maximum propagation time, and time delay extension of the 95% total power of the six links. The results calculated by the RTBS_ERA5 are all greater than the Bello model, and the further distance and wider beam, the more pronounced the effect of path bending and delay. The errors between RTBS_ERA5 and Bello are on a microsecond scale. It is clear that the RTBS _ERA5 model is more precise than the Bello model and is better suited to situations where accurate estimates of transmission delay are required.

D. Analysis of Daily Propagation Delay of RTBS_ERA5

The LT1441 and LT2305 links are selected to calculate the hour-by-hour propagation delays on August 25–27, 2020, based on ERA5 meteorological data. Two links parameters except for the location and altitude of the transmitter and receiver are set to the same: frequency 4.09 GHz, transmitting and receiving antenna height 5.2 m, elevation angle 20 mrad, total transmitting and receiving gain 97 dB, and the rest of the link parameters refer to the Appendix.

The hour-by-hour normalized delay power spectra thermal maps of the two links are given in Fig. 12. As seen from Fig. 12, the RTBS_ERA5 extracts the hour-by-hour propagation delay variation characteristics. The LT1441 link is affected by the marine climate, and the meteorological environment is complex and variable. The propagation delay is less regular and more random. As shown in Fig. 12(a), from 19:00 to 23:00 on the 25th, the delay power spectrum has a sudden shift within a short period, which was in fact caused by sudden changes in the meteorological environment. The temperature

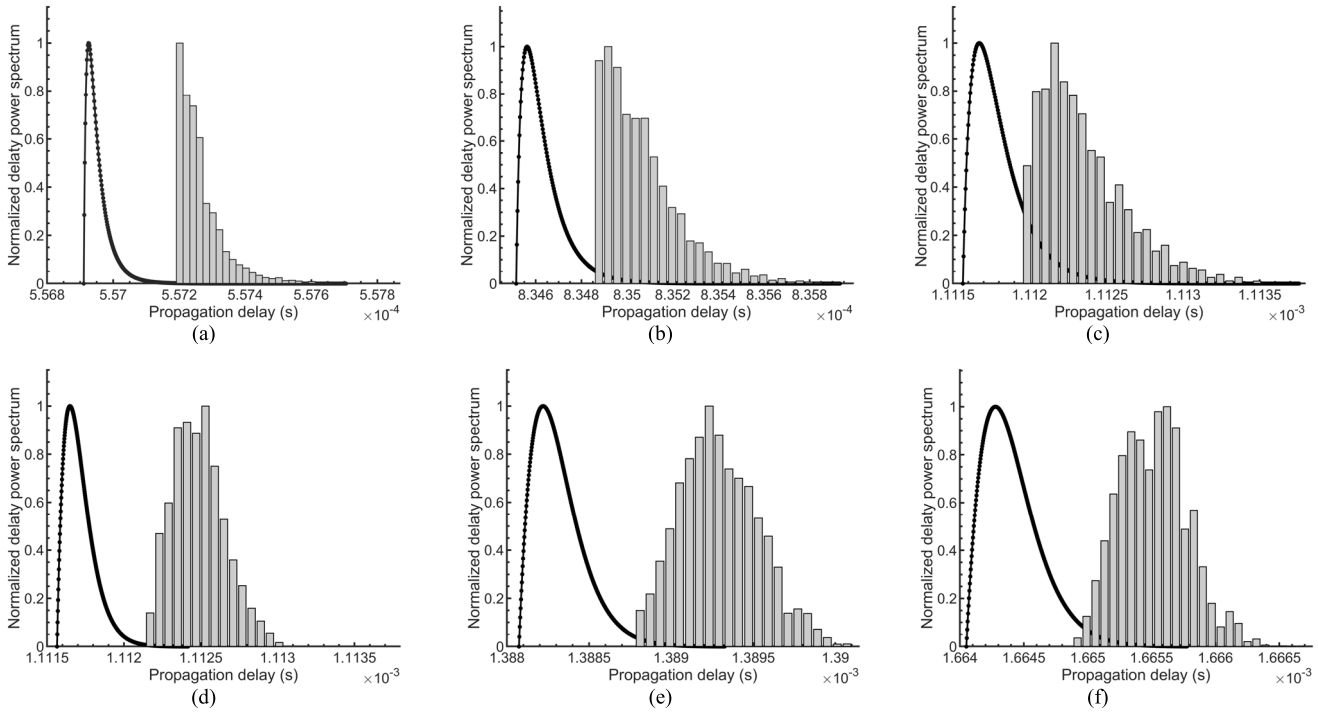

Fig. 11. Normalized delayed power spectra of scattered links with different distances and beamwidths are calculated using the RTBS_ERA5 model (histogram) and Bello model (dot plot). (a) Path 1. (b) Path 2. (c) Path 3. (d) Path 4. (e) Path 5. (f) Path 6.

TABLE IV
STATISTICAL RESULTS OF PROPAGATION TIME AT 95% OF TOTAL POWER (s)

Path	RBM_ERA5			Bello			RBM_ERA5 - Bello		
	Min propagation time	Max propagation time	Time delay extension	Min propagation time	Max propagation time	Time delay extension	Min propagation time error	Max propagation time error	Time delay extension error
1	5.5720e-04	5.5742e-04	2.1842e-07	5.5691e-04	5.5703e-04	1.1914e-07	2.9088e-07	3.9017e-07	9.9284e-08
2	8.3488e-04	8.3541e-04	5.3557e-07	8.3451e-04	8.3482e-04	3.0919e-07	3.6300e-07	5.8938e-07	2.2638e-07
3	1.1120e-03	1.1129e-03	9.4446e-07	1.1116e-03	1.1122e-03	6.0064e-07	4.1852e-07	7.6233e-07	3.4381e-07
4	1.1122e-03	1.1128e-03	6.5414e-07	1.1116e-03	1.1119e-03	3.4435e-07	6.0583e-07	9.1561e-07	3.0979e-07
5	1.3888e-03	1.3898e-03	9.5397e-07	1.3881e-03	1.3886e-03	5.5385e-07	7.3870e-07	1.1388e-06	4.0012e-07
6	1.6649e-03	1.6660e-03	1.1030e-06	1.6640e-03	1.6649e-03	8.1199e-07	8.7157e-07	1.1625e-06	2.9097e-07

TABLE V
STATISTICAL RESULTS OF THE TIME DELAY EXTENSION AND THE LONGEST AND SHORTEST PROPAGATION TIME FOR TWO LINKS (s)

	Path 1441			Path 2305		
	Time delay extension	Min propagation time	Max propagation time	Time delay extension	Min propagation time	Max propagation time
Max	3.327e-07	9.249926e-04	9.253203e-04	2.388e-07	7.521683e-04	7.524055e-04
Min	3.189e-07	9.249436e-04	9.252654e-04	2.263e-07	7.521329e-04	7.523604e-04
Max-Min	1.38e-08	4.90e-08	5.49e-08	1.25e-08	3.53e-08	4.51e-08

gradient in the vertical direction of the common scatterer of the low elevation subbeam changes from −5e-3 °C/m to −3e-3 °C/m, resulting in a reduction in the received power of the low elevation subbeam whose propagation time is shorter, which is reflected in the normalized delayed power spectrum thermogram as a shift of the maximum received power peak toward the region with a longer propagation time.

The meteorological environment of the LT2305 link is relatively stable, and the propagation delay shows a more apparent diurnal variation pattern. The propagation time becomes longer during the day and shorter during the night and the diurnal propagation time variation of about tens of nanoseconds within 24 h. Table V gives the statistical results of the time delay extension, the longest and shortest propagation time

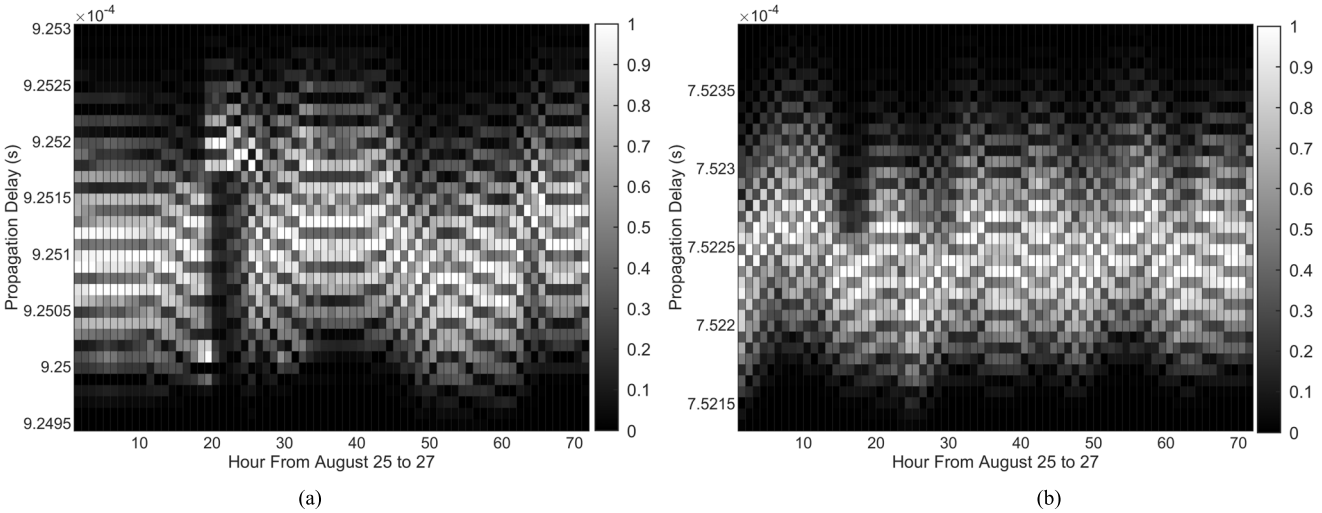

Fig. 12. Hourly normalized delayed power spectrum thermal maps for (a) LT1441 and (b) LT2305.

TABLE VI
PART I PARAMETERS OF TEN LINKS FROM THE REPORT OT/TRER 16

Path	Transmitter latitude (°)	Transmitter longitude (°)	Receiver latitude (°)	Receiver longitude (°)	Frequency（MHz）	Transmitter antenna height (m)	Receiver antenna height (m)	Transmitter elevation (mrad)	Receiver elevation (mrad)	Total antenna gain (dB)
LT0908	40.3919	285.8131	41.54	289.0689	3670	9.1	2.7	-2.2	7.1	95
LT1440	51.3486	304.3792	48.9503	305.4194	505	5.2	5.2	17.6	18.7	61
LT1441	51.3486	304.3792	48.9503	305.4194	4090	5.2	5.2	-3.2	-2	97
LT2063	50.227	356.339	51.563	359.704	9640	4.9	57.9	5.6	6.1	73
LT2272	35.7069	139.4919	38.2808	140.8264	599	28	15	7	10.9	71
LT2273	35.7069	139.4919	38.2808	140.8264	2120	28	15	-2.8	1.1	94
LT2304	35.7067	139.4883	38.5728	140.9642	600	47	3	24.9	32.9	56
LT2305	35.7067	139.4883	37.5931	140.4172	600	47	3	24.9	30	56
LT2306	35.7067	139.4883	38.5728	140.9642	2120	28	5	0	11.3	79
LT2307	35.7067	139.4883	37.5931	140.4172	2120	28	3	2.1	6.7	79

TABLE VII
PART II PARAMETERS OF TEN LINKS FROM THE REPORT OT/TRER 16

Path	climate zone	Distance (km)	Loss relative to free space (dB)	Altitude of transmitter (m)	Altitude of receiver (m)	Altitude of transmitter obstacle (m)	transmitter obstacle distance (km)	Altitude of receiver obstacle (m)	receiver obstacle distance (km)	K
LT0908	0	301.87	78.1	109	15	2	49	11	5.6	1.447
LT1440	0	276.95	66.9	108	143	0	44.4	76	35.5	1.396
LT1441	0	276.95	84	108	143	0	44.4	76	35.5	1.396
LT2063	7	278.8	70.4	128	97	287	94	95	36	1.419
LT2272	6	309.96	70.8	75	225	14	35.9	265	9.8	1.422
LT2273	6	309.96	73.5	75	225	14	35.9	265	9.8	1.422
LT2304	6	344.7	69	75	21	13	45.7	80	8	1.418
LT2305	6	225.67	61.2	75	342	17	50.9	470	45	1.421
LT2306	6	344.7	90.3	75	21	16	34.6	360	38.6	1.418
LT2307	6	225.67	68.3	75	342	16	34.5	470	45	1.421

for two links. As can be seen from Table V, the meteorological environment has an important influence on the propagation time of troposcatter. Over a propagation distance of 200–300 km, the propagation time and time delay extension fluctuate by tens of nanoseconds in different meteorological conditions, and the magnitude of the fluctuation increases with distance. The intensity of the fluctuation is closely related to the meteorological environment along the propagation path.

VII. CONCLUSION

In order to address the problem that the existing troposcatter model cannot accurately portray the influence of meteorological environments on transmission loss and propagation

delay, this article proposes a troposcatter loss and delay estimation model RTBS_ERA5, which is based on the 3-D ray-tracing and beam splitting with the ERA5 reanalysis data. The construction method of the model is given. The ITU model, report OT/TRER 16, and the Bello model are used for comparative and validation. Finally, the daily variation characteristics of loss and delay are analyzed. The study results show that RTBS_ERA5 can accurately estimate transmission loss, propagation time, and time delay extension based on ERA5 reanalysis data and provide an accurate link performance analysis tool for wireless communication systems, high-precision time synchronization systems, over-the-horizon detection, and positioning systems based on troposcatter links. Nevertheless, we noted that the meteorological data of ERA5 are nonreal-time reanalysis data, which generally have a five-day delay, and the RTBS_ERA5 is currently only capable of postanalysis. Further research will validate the use of reliable numerical weather prediction models for forecasting functions.

APPENDIX

See Table VI and Table VII.

ACKNOWLEDGMENT

Shuang Zhang would like to thank ITU and China Research Institute of Radiowave Propagation (CRIRP) for supporting the database about the propagation and the European Centre for Medium-Range Weather Forecasts (ECMWF) for providing meteorological data. He would also like to thank Dr. Pei-Pei Wei for her valuable discussions and Dr. Lei Li for his helpful messages. The authors would like to thank the editors and reviewers for their constructive comments.

REFERENCES

[1] C. L. Li, X. H. Chen, and X. P. Liu, "Cognitive tropospheric scatter communication," *IEEE Trans. Veh. Technol.*, vol. 67, no. 2, pp. 1482–1491, Feb. 2018.

[2] E. Dinc and O. B. Akan, "Fading correlation analysis in MIMO-OFDM troposcatter communications: Space, frequency, angle and space-frequency diversity," *IEEE Trans. Commun.*, vol. 63, no. 2, pp. 476–486, Feb. 2015.

[3] E. Dinc and O. B. Akan, "More than the eye can see: Coherence time and coherence bandwidth of troposcatter links for mobile receivers," *IEEE Veh. Technol. Mag.*, vol. 10, no. 2, pp. 86–92, Jun. 2015.

[4] C. Li and X. Chen, "Beyond line-of-sight two-way time synchronisation via troposcatter," *Electron. Lett.*, vol. 52, no. 25, pp. 2067–2068, Dec. 2016.

[5] J. Liuv and X. Chen, "Time synchronisation for multi-static radar via microwave and troposcatter," *J. Eng.*, vol. 2018, no. 1, pp. 39–41, Jan. 2018.

[6] Z. Liu, X. Chen, and Q. Liu, "Research on passive troposcatter location system," *Radioengineering*, vol. 28, no. 1, pp. 312–319, Apr. 2019.

[7] X. Mi, Z. Liu, X. Chen, and Q. Liu, "An efficient DOA estimation method for passive surveillance system based on troposcatter," *Math. Problems Eng.*, vol. 2021, pp. 1–7, Mar. 2021.

[8] M. Zhang, "Chapter II troposcatter propagation mechanism," in *Tropospheric Scattering Propagation*. Beijing, China: House of Electronics Industry, 2004, pp. 8–25.

[9] C. Li, X. Chen, and Z. Xie, "A closed-form expression of coherence bandwidth for troposcatter links," *IEEE Commun. Lett.*, vol. 22, no. 3, pp. 646–649, Mar. 2018.

[10] Z. Xie, X. Chen, and X. Liu, "A virtual pilot-assisted channel estimation algorithm for MIMO-SCFDE systems over fast time-varying multipath channels," *IEEE Trans. Veh. Technol.*, vol. 67, no. 6, pp. 4901–4909, Jul. 2018.

[11] *Data Banks Used for Testing Prediction Methods*, document 5/378, CCIR, 1982.

[12] A. G. Longley and R. K. Reasoner, "Comparison of propagation measurements with predicted values in the 20 to 10, 000 MHz range," ITS, Chennai, India, Tech. Rep. OT/TRER, Jul. 1971.

[13] *Transmission Loss Predictions for Tropospheric Communication Circuits*, document 101, NBS, 1967.

[14] J. Battesti, L. Boithias, and P. Misme, "Calcul des affaiblissements en propagation transhorizon à partir des paramètres radiométéorologiques," *Ann. Télécommun.*, vol. 23, nos. 5–6, pp. 129–140, May 1968.

[15] *Propagation Prediction Techniques and Data Required for the Design of Trans-Horizon Radio-Relay Systems*, document ITU-R P.617-1, Geneva, Switzerland, 1992.

[16] *Propagation Prediction Techniques and Data Required for the Design of Trans-Horizon Radio-Relay Systems*, document ITU-R P.617-5, Geneva, Switzerland, 2019.

[17] L. Li, L.-K. Lin, Z.-S. Wu, and Z.-W. Zhao, "Study on the maximum calculation height and the maximum propagation angle of the troposcatter wide-angle parabolic equation method," *IET Microw., Antennas Propag.*, vol. 10, no. 6, pp. 686–691, Sep. 2016.

[18] E. Dinc and O. B. Akan, "A ray-based channel model for MIMO troposcatter communications," in *Proc. IEEE 24th Annu. Int. Symp. Pers., Indoor, Mobile Radio Commun. (PIMRC)*, Sep. 2013, pp. 243–247.

[19] E. Dinc and O. B. Akan, "A ray-based channel modeling approach for MIMO troposcatter beyond-line-of-sight (b-LoS) communications," *IEEE Trans. Commun.*, vol. 63, no. 5, pp. 1690–1699, Mar. 2015.

[20] L. Li, Z.-S. Wu, L.-K. Lin, R. Zhang, and Z.-W. Zhao, "Study on the prediction of troposcatter transmission loss," *IEEE Trans. Antennas Propag.*, vol. 64, no. 3, pp. 1071–1079, Mar. 2016.

[21] P. Wei, X. Du, and C. Jiang, "Study on tropospheric scatter beyond-line-of-sight channel transmission loss for short-term and long-term fading," *J. Electron. Inf. Technol.*, vol. 40, no. 7, pp. 1745–1751, Jul. 2018.

[22] D. Yuan and X. Chen, "Troposcatter transmission loss prediction based on particle swarm optimisation," *IET Microw., Antennas Propag.*, vol. 15, no. 3, pp. 332–341, Feb. 2021.

[23] E. D. Sunde, "Digital troposcatter transmission and modulation theory," *Bell Syst. Tech. J.*, vol. 43, no. 1, pp. 143–214, Jan. 1964.

[24] P. Bello, "A troposcatter channel model," *IEEE Trans. Commun.*, vol. COM-17, no. 2, pp. 130–137, Apr. 1969.

[25] H. Hersbach *et al.*, "The ERA5 global reanalysis," *Quart. J. Roy. Meteorol. Soc.*, vol. 146, no. 730, pp. 1999–2049, Jun. 2020.

[26] *Copernicus Climate Change Service ERA5: What is the Spatial Reference*. Accessed: Mar. 4, 2021. [Online]. Available: https://confluence.ecmwf.int/display/CKB/ERA5%3A+What+is+the+spatial+reference

[27] T. Hobiger, R. Ichikawa, Y. Koyama, and T. Kondo, "Fast and accurate ray-tracing algorithms for real-time space geodetic applications using numerical weather models," *J. Geophys. Res.*, vol. 113, no. 20, pp. 165–179, Oct. 2008.

[28] Y. Yao, C. Xu, J. Shi, N. Cao, B. Zhang, and J. Yang, "ITG: A new global GNSS tropospheric correction model," *Sci. Rep.*, vol. 5, Aug. 2015, Art. no. 10273.

[29] J. Böehm, R. Heinkelmann, and H. Schuh, "Short note: A global model of pressure and temperature for geodetic applications," *J. Geodesy*, vol. 81, no. 10, pp. 679–683, Oct. 2007.

[30] ECMWF. *IFS Documentation Part I: Observations*. Accessed: Sep. 1, 2020. [Online]. Available: https://www.ecmwf.int/node/19745

[31] D. A. Spera and T. R. Richards, "Modified power law equations for vertical wind profiles," in *Proc. Wind Characteristics Wind Energy Siting Conf.*, OR, USA, Jun. 1979.

[32] M. Jean, "Refractive index formulae for radio waves," in *Proc. FIG Int. Congr.*, Washington, DC, USA, 2002, pp. 19–26.

[33] G. D. Thayer, "An improved equation for the radio refractive index of air," *Radio Sci.*, vol. 9, no. 10, pp. 803–807, 1974.

[34] Z. Di, "The study of the GNSS tropospheric zenith delay model and mapping function," Ph.D. dissertation, Dept. Geodesy and Geomatics. Wuhan Univ., Wuhan, China, 2017.

[35] V. Nafisi *et al.*, "Comparison of ray-tracing packages for troposphere delays," *IEEE Trans. Geosci. Remote Sens.*, vol. 50, no. 2, pp. 469–481, Aug. 2011.

[36] R. Zheng, "Geometrical optics," in *Fundamentals of Electromagnetic Ray Theory* Chengdu, China: Institute of Telecommunications Engineering Press, 1989, pp. 90–95.

[37] D. Eriksson, D. S. Macmillan, and J. M. Gipson, "Tropospheric delay ray tracing applied in VLBI analysis," *J. Geophys. Research: Solid Earth*, vol. 119, no. 12, pp. 9156–9170, Dec. 2014.

[38] H. Jie, "Parctical method of atmospheric refractive correction," in *Correction for Atmospheric Refractive Error of Radio Wave*. Beijing, China: National Defence Industry Press, 1999, pp. 101–103.
[39] V. Tatarski, *Wave Propagation in a Turbulent Medium*. New York, NY, USA: McGraw-Hill, 1961.
[40] F. H. Ruggiero and D. A. DeBenedictis, "Forecasting optical turbulence from mesoscale numerical weather prediction models," in *Proc. DOD High Perform. Comput. Users Group Conf.*, Austin TX, USA, 2002, pp. 10–14.
[41] A. Ishimaru, "Scattering of waves from the tenuous distribution of particles," in *Wave Propagation and Scattering in Random Wave Propagation and Scattering in Random Media*. New York, NY, USA: Academic, 1978, pp. 74–75.
[42] *Attenuation by Atmospheric Gases and Related Effects*, document ITU-R P.676-12, Geneva, Switzerland, Aug. 2019.

Shuang Zhang was born in Sichuan, China, in 1990. He received the M.S. degree from the Air and Missile Defense College, Air Force Engineering University, Xi'an, China, in 2014, where he is currently pursuing the Ph.D. degree in arms science and technology.

His research interests include troposcatter propagation and troposcatter positioning.

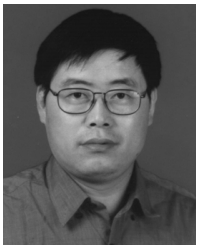

Xi-Hong Chen was born in Shaanxi, China, in 1961. He received the M.S. degree from Xidian University, Xi'an, China, in 1986, and the Ph.D. degree from the Air and Missile Defense College, Air Force Engineering University, Xi'an, in 2010.

He is currently with the Air and Missile Defense College. His research interests include troposcatter communication, high-precision time synchronization based on troposcatter, and passive detection based on troposcatter.

Qiang Liu was born in Hunan, China, in 1985. He received the M.S. and Ph.D. degrees from the Air and Missile Defense College, Air Force Engineering University, Xi'an, China, in 2010 and 2014, respectively.

He is currently with the Air and Missile Defense College. His research interests include troposcatter communication and high-precision time synchronization based on troposcatter.

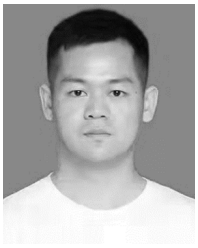

Xin-Ping Mi was born in Gansu, China, in 1997. He received the M.S. degree from the Air and Missile Defense College, Air Force Engineering University, Xi'an, China, in 2021.

His research interests include troposcatter communication and passive detection based on troposcatter.